PERGAMON

International Journal of Impact Engineering 24 (2000) 403–415

INTERNATIONAL JOURNAL OF IMPACT ENGINEERING

www.elsevier.com/locate/ijimpeng

On the optimal nose geometry for a rigid penetrator, including the effects of pressure-dependent friction

S.E. Jones[a,*,1], William K. Rule[b]

[a]U.S. Air Force Research Laboratory, Munitions Directorate, Eglin AFB, FL, USA
[b]Trus Joist MacMillan, Boise, ID, USA

Received 10 March 1998; accepted 22 August 1998

Abstract

In a related paper (Jones et al., Comput Mech, 1998;22:413) the problem of maximizing the depth of penetration by a normally impacting cylindrical projectile by optimizing the nose geometry was considered. These results were accomplished by neglecting any frictional resistance offered by the target and only considering the normal pressure acting against the penetrator nose. The problem of maximizing the penetration depth achieved by the normal impact of a cylindrical projectile including the effects of friction acting on the penetrator nose is a much more challenging problem. In this paper, the normal impact and penetration problem is considered including the effects of pressure-dependent friction.

1. Introduction

In an earlier paper, Jones et al. [1] presented the nose geometry for a normal impacting, rigid projectile that maximizes penetration depth. This problem was solved by neglecting all forms of friction that act on the penetrator nose. By assuming that the pressure that acts on the nose of the penetrator is of Poncelet form [2] (see also [3,4, p. 15] or [5, pp. 200, 210]), it was shown that the nose had a fairly simple geometry. In spite of the simplicity of this result, it is surprising that the optimal geometry had a blunt nose regardless of the nose length.

For moderate to low impact velocities there seemed to be little to gain from the optimal geometry over most others. However, at very high impact velocities (say, those in excess of 1000 m/s), substantial differences could be noted in penetration depth when compared to other conventional geometries. As indicated earlier, the projectile impacts normally and it is assumed

* Corresponding author.
[1] On leave from the University of Alabama.

0734-743X/00/$ - see front matter
PII: S0734-743X(99)00157-8

that the energy level is high enough to neglect any of the effects associated with entry into the target.

There has been much effort directed toward understanding the various forms that friction can take (e.g., [6] or [7]). This is a very complicated problem, especially when high sliding speeds are involved (e.g., [8–10]). Very little appears to be known about the friction that acts on bodies during high velocity penetration. However, evidence points toward some pressure dependence with a reduced coefficient of friction. The simplest form that such friction can take is that which is proportional to the pressure, similar to classical Coulomb friction. Other forms have been proposed (e.g., [9]) and these could be incorporated into the analysis presented in this paper with more difficulty. The present effort utilizes a friction force that is proportional to the pressure and this has a substantial effect on the results. Some unexpected complexities make any form of approximate solution practically impossible. A numerical study of the solutions to the Euler–Lagrange equation is performed. The results are both interesting and useful.

2. Force of resistance on the projectile

Consider a rigid axisymmetric projectile normally penetrating a semi-infinite target. The cross-section of the tip is shown in Fig. 1. The length of the nose is b and the radius of the shank of the projectile is a. For all acceptable nose geometries $y = y(x)$, $y(0) = 0$ and $y(b) = a$. We assume in this analysis that the effects of friction are negligible beyond the nose at $x = b$.

The increment of force resisting the motion of the projectile is

$$dF = 2\pi y(\, p \sin\theta + f \cos\theta)\, ds, \tag{1}$$

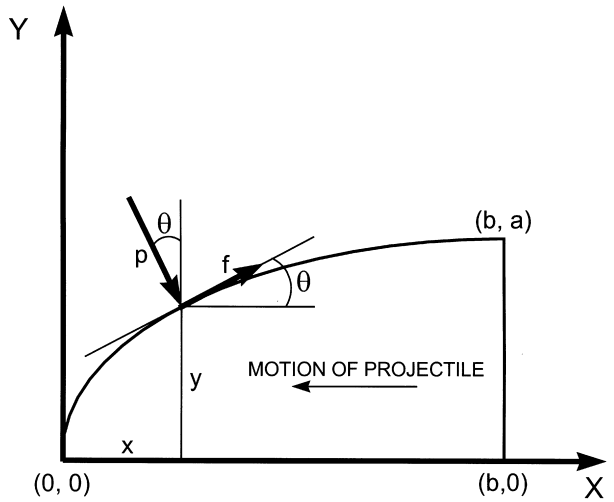

Fig. 1. Cross-section of the nose of an axisymmetric penetrator. The penetrator is acted upon by a continuous pressure p and friction (per unit area) f. The length of the nose of the projectile is b and the radius of the shank is a.

where

$$ds = \sqrt{1 + y'^2}\, dx \tag{2}$$

is the increment of arc length on the surface of the nose. From the geometry in Fig. 1, it is easy to see that

$$y' = \tan\theta, \tag{3}$$

$$\sin\theta = \frac{y'}{\sqrt{1 + y'^2}} \tag{4}$$

and

$$\cos\theta = \frac{1}{\sqrt{1 + y'^2}}. \tag{5}$$

Substituting Eqs. (2), (4) and (5) into Eq. (1), we find

$$dF = 2\pi y(y'p + f)\, dx \tag{6}$$

which can be integrated between $x = 0$ and b to give the net force F resisting the motion of the projectile

$$F = 2\pi \int_0^b (yy'p + yf)\, dx. \tag{7}$$

3. Friction on the projectile

There are a number of forms that friction may take. Among the simplest for this problem is friction proportional to the normal pressure p. Take the coefficient of friction to be μ and

$$f = \mu p. \tag{8}$$

As we assumed in our previous paper [1], the pressure p is of the Poncelet type

$$p = Av^2 \sin^2\theta + B, \tag{9}$$

where A and B are constants, v is the current axial velocity of the projectile, and $v\sin\theta$ is the normal component of axial velocity contributing to the pressure at the surface of the nose (see [3]). Now, substituting Eqs. (8) and (9) into Eq. (7), we find

$$F = 2\pi \int_0^b \left[Av^2 y \frac{y'^3 + \mu y'^2}{1 + y'^2} + B(yy' + \mu y) \right] dx, \tag{10}$$

where $\sin\theta$ in Eq. (9) has been replaced by the right-hand side of Eq. (4).

When $\mu = 0$ in Eq. (10), we return to the problem considered in [1] in which the net resistive force has the form

$$F = 2\pi Av^2 \int_0^b \frac{yy'^3}{1 + y'^2}\, dx + \pi a^2 B \tag{11}$$

and it is easy to see that maximum depth of penetration can be achieved when the integral I

$$I = \int_0^b \frac{yy'^3}{1+y'^2}\,\mathrm{d}x \tag{12}$$

is a minimum, because F is a minimum. However, when friction is included it is not so easy to see which geometry will optimize the depth of penetration looking at Eq. (10).

4. Maximum penetration depth

The equation of motion of the projectile is

$$\begin{aligned} m\dot{v} &= -F \\ &= -\pi a^2(ANv^2 + BM), \end{aligned} \tag{13}$$

where m is the projectile mass and

$$\begin{aligned} N &= \frac{2}{a^2}\int_0^b y\,\frac{y'^3+\mu y'^2}{1+y'^2}\,\mathrm{d}x \\ &= 2\alpha\int_0^1 z\,\frac{\alpha z'^3+\mu z'^2}{1+\alpha^2 z'^2}\,\mathrm{d}\xi \end{aligned} \tag{14}$$

and

$$\begin{aligned} M &= 1+\frac{2\mu}{a^2}\int_0^b y\,\mathrm{d}x \\ &= 1+\frac{2\mu}{\alpha}\int_0^1 z\,\mathrm{d}\xi. \end{aligned} \tag{15}$$

In the last two equations, $x = b\xi$, $y = az$, $\alpha = a/b$, where $z = z(\xi)$ and ξ are dimensionless variables with $z(0) = 0$ and $z(1) = 1$.

Because N and M are time-independent functions, Eq. (13) can be simply integrated, which leads to

$$P = \frac{m}{2\pi a^2 AN}\ln\left(1+\frac{AN}{BM}v_0^2\right), \tag{16}$$

where P is the penetration depth. In order to find the geometry that maximizes P, we must vary z in Eqs. (14) and (15) for each fixed value of α and μ. Suppose that $z = w(\xi)$ maximizes P in Eq. (16). Consider variations of this path with

$$z = w + \varepsilon\eta, \tag{17}$$

where ε is a parameter and $\eta = \eta(\xi)$ is any differentiable function with $\eta(0) = \eta(1) = 0$. Substituting Eq. (17) into Eqs. (14) and (15), we see that $N = N(\varepsilon)$ and $M = M(\varepsilon)$. Further, it is now clear from Eq. (16) that $P = P(\varepsilon)$ with $\max P = P(0)$. Hence, it follows that $\mathrm{d}P/\mathrm{d}\varepsilon = 0$ at $\varepsilon = 0$.

By differentiating Eq. (16) with respect to ε, we find

$$\frac{\mathrm{d}P}{\mathrm{d}\varepsilon} = \frac{-m}{2\pi a^2 AN^2}\left\{\left[\ln\left(1+\frac{AN}{BM}v_0^2\right) - \frac{(AN/BM)v_0^2}{1+(AN/BM)v_0^2}\right]\frac{\mathrm{d}N}{\mathrm{d}\varepsilon} + \frac{Av_0^2}{B}\,\frac{N^2}{M^2}\,\frac{1}{1+(AN/BM)v_0^2}\,\frac{\mathrm{d}M}{\mathrm{d}\varepsilon}\right\}. \tag{18}$$

The derivatives $\mathrm{d}N/\mathrm{d}\varepsilon$ and $\mathrm{d}M/\mathrm{d}\varepsilon$ can be found by differentiating Eqs. (14) and (15)

$$\frac{\mathrm{d}N}{\mathrm{d}\varepsilon} = 2\alpha\int_0^1 \eta\left[\frac{\partial\phi}{\partial z} - \frac{\mathrm{d}}{\mathrm{d}\xi}\left(\frac{\partial\phi}{\partial z'}\right)\right]\mathrm{d}\xi, \tag{19}$$

where

$$\phi(z,z') = z\,\frac{\alpha z'^3 + \mu z'^2}{1+\alpha^2 z'^2} \tag{20}$$

and

$$\frac{\mathrm{d}M}{\mathrm{d}\varepsilon} = \frac{2\mu}{\alpha}\int_0^1 \eta\,\mathrm{d}\xi. \tag{21}$$

In Eqs. (19) and (20), $z' = \mathrm{d}z/\mathrm{d}\xi$. Now, substituting Eqs. (19) and (21) into Eq. (18) and computing $\lim_{\varepsilon\to 0}\mathrm{d}P/\mathrm{d}\varepsilon = 0$, leads to

$$2\alpha\left[\ln\left(1+\lambda\frac{\bar N}{\bar M}\right) - \frac{\lambda\bar N/\bar M}{1+\lambda\bar N/\bar M}\right]\int_0^1\eta\left[\frac{\partial\phi}{\partial w} - \frac{\mathrm{d}}{\mathrm{d}\xi}\left(\frac{\partial\phi}{\partial w'}\right)\right]\mathrm{d}\xi + \frac{2\mu}{\alpha}\lambda\,\frac{\bar N^2}{\bar M^2}\,\frac{1}{1+\lambda\bar N/\bar M}\int_0^1\eta\,\mathrm{d}\xi$$
$$= \int_0^1\left\{2\alpha\left[\ln(1+\lambda\bar N/\bar M) - \frac{\lambda\bar N/\bar M}{1+\lambda\bar N/\bar M}\right]\left[\frac{\partial\phi}{\partial w} - \frac{\mathrm{d}}{\mathrm{d}\xi}\left(\frac{\partial\phi}{\partial w'}\right)\right] + \frac{2\mu}{\alpha}\lambda\,\frac{\bar N^2}{\bar M^2}\,\frac{1}{1+\lambda\bar N/\bar M}\right\}\mathrm{d}\xi = 0, \tag{22}$$

where

$$\bar N = 2\alpha\int_0^1 w\,\frac{\alpha w'^3 + \mu w'^2}{1+\alpha^2 w'^2}\,\mathrm{d}\xi \tag{23}$$

and

$$\bar M = 1 + \frac{2\mu}{\alpha}\int_0^1 w\,\mathrm{d}\xi \tag{24}$$

and $\lambda = Av_0^2/B$. Because Eq. (22) must hold for all admissible variations η on the interval $0 \leqslant \xi \leqslant 1$ with $\eta(0) = \eta(1) = 0$, it follows that w satisfies

$$\alpha^2\left[\ln\left(1+\lambda\frac{\bar N}{\bar M}\right) - \frac{\lambda\bar N/\bar M}{1+\lambda\bar N/\bar M}\right]\left[\frac{\partial\phi}{\partial w} - \frac{\mathrm{d}}{\mathrm{d}\xi}\left(\frac{\partial\phi}{\partial w'}\right)\right] + \mu\lambda\,\frac{\bar N^2}{\bar M^2}\,\frac{1}{1+\lambda\bar N/\bar M} = 0. \tag{25}$$

This equation is the Euler–Lagrange equation for the variational problem described by Eq. (16). It is far more complicated than the usual Euler–Lagrange equation because $\bar{N}$ and $\bar{M}$ involve integrals of the dependent variable w from Eqs. (23) and (24). Additionally, referring back to the definition of ϕ in Eq. (20), we can expand the derivatives indicated in Eq. (25) to get

$$\frac{\partial\phi}{\partial w} - \frac{\mathrm{d}}{\mathrm{d}\xi}\left(\frac{\partial\phi}{\partial w'}\right) = \frac{\mu\alpha^2 w'^4 - 2\alpha w'^3 - \mu w'^2}{(1+\alpha^2 w'^2)^2} + ww'' \frac{2\alpha^3 w'^3 + 6\mu\alpha^2 w'^2 - 6\alpha w' - 2\mu}{(1+\alpha^2 w'^2)^3}, \tag{26}$$

where $w' = \mathrm{d}w/\mathrm{d}\xi$ and $w'' = \mathrm{d}^2 w/\mathrm{d}\xi^2$. This means that not only are there integrals of the dependent variable and its derivative in Eq. (25), but there are also derivatives through the second order. Eq. (25) is a nonlinear differential–integral equation of extraordinary complexity to be solved subject to the two-point boundary conditions $w(0) = 0$ and $w(1) = 1$. There may be some useful approximations to this problem, but in the interests of expedience we will pass up this approach and solve the problem numerically.

Before turning to the solution of Eq. (25), we should note that it reduces to the Euler–Lagrange equation for the frictionless case [1] when $\mu = 0$. When $\mu \to 0$, the second term in Eq. (25) vanishes, while $\bar{M} \to 1$ and

$$\bar{N} \to 2\alpha^2 \int_0^1 \frac{ww'^3}{1+\alpha^2 w'^2}\,\mathrm{d}\xi. \tag{27}$$

This leaves us with the product

$$\alpha^2\left[\ln(1+\lambda\bar{N}) - \frac{\lambda\bar{N}}{1+\lambda\bar{N}}\right]\left[\frac{\partial\phi}{\partial w} - \frac{\mathrm{d}}{\mathrm{d}\xi}\left(\frac{\partial\phi}{\partial w'}\right)\right] = 0 \tag{28}$$

with

$$\frac{\partial\phi}{\partial w} - \frac{\mathrm{d}}{\mathrm{d}\xi}\left(\frac{\partial\phi}{\partial w'}\right) = \frac{-2\alpha w'^3}{(1+\alpha^2 w'^2)^2} + ww'' \frac{2\alpha^3 w'^3 - 6\alpha w'}{(1+\alpha^2 w'^2)^3}. \tag{29}$$

For $\alpha^2 \neq 0$ and $\bar{N} > 0$, the first of the two factors in Eq. (28) does not vanish. This leaves only the second factor to satisfy Eq. (28). Hence, the factor shown in Eq. (29) must equal zero and this is the Euler–Lagrange equation presented in [1] for the frictionless case.

5. Numerical solution methodology

A numerical solution for Eq. (25) was obtained by assuming a solution of the following form:

$$z = a_1\xi^n + a_2\xi^{2n} + a_3\xi^{3n}, \tag{30}$$

where a_i and n are adjustable parameters which are a function of α, λ, and μ. A least-squares approach was used to obtain values for these parameters. For particular α, λ, and μ values, Eq. (25) was evaluated [using the assumed function, Eq. (30)] at 20 evenly spaced ξ values from 0.05 to 1. These 20 function values (which ideally should equal zero) were then squared and summed to produce an aggregate fit error. An optimizer was used to adjust the a_i and n values to minimize the

fit error. Values of the $\bar{N}$ [Eq. (23)] and $\bar{M}$ [Eq. (24)] integrals for insertion into Eq. (25) were obtained by a numerical integration scheme also using 20 evenly spaced ξ values from 0.05 to 1. The optimizer was constrained to seek solutions with z and z' greater than or equal to zero. Further, the parameter n of Eq. (30) was forced to be positive. These calculations were conveniently conducted using a spreadsheet computer program.

It must be noted that the development of Eq. (25) is a necessary, but not sufficient, condition for maximum penetration depth. It can equally apply to minimum penetration depth. In fact, both maxima and minima are achieved along the same path for different combinations of the physical parameters α, λ, and μ. This will be illustrated in the next section.

6. Typical results

Numerical test cases were investigated using the same model parameters as reported by Forrestal et al. [11] for test results involving firing small steel projectiles into semi-infinite grout

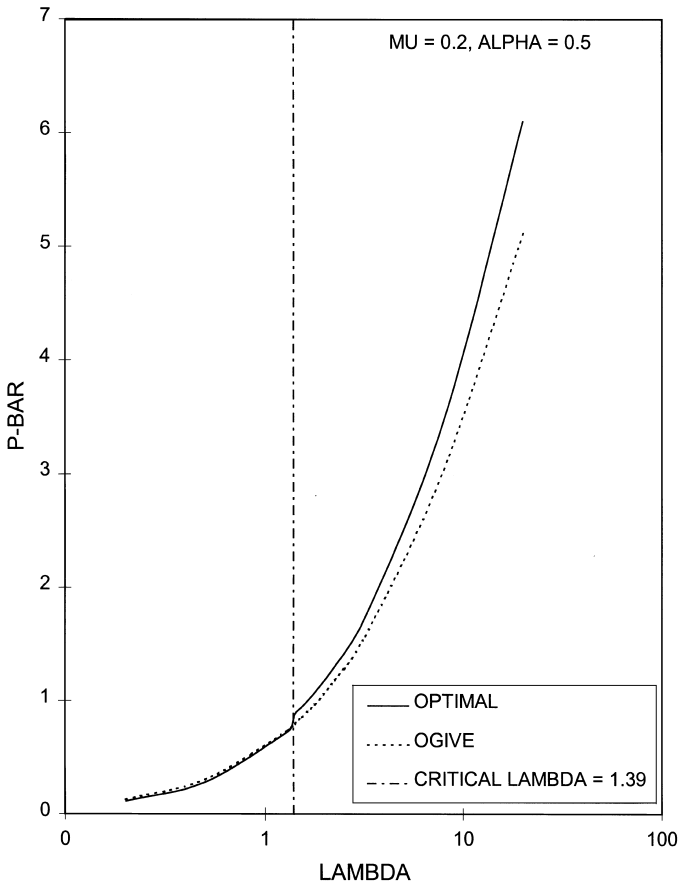

Fig. 2. Plot of $\bar{P}$ versus λ for optimal and ogival nose shapes. Note that the optimal nose goes blunt (penetration depth minimized) for λ values less than 1.39 for this case ($\alpha = 0.5$, $\mu = 0.2$).

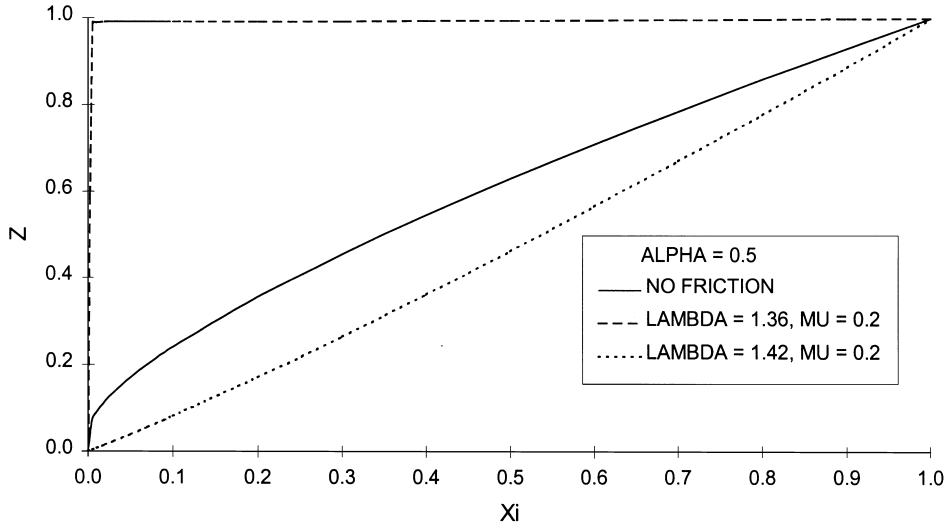

Fig. 3. Comparison of optimal nose shapes with the frictionless optimal nose shape of [1]. For the $\lambda = 1.42$ case penetration depth is maximized and ogival performance is bettered. Penetration depth is minimized for the $\lambda = 1.36$ case (nose blunted).

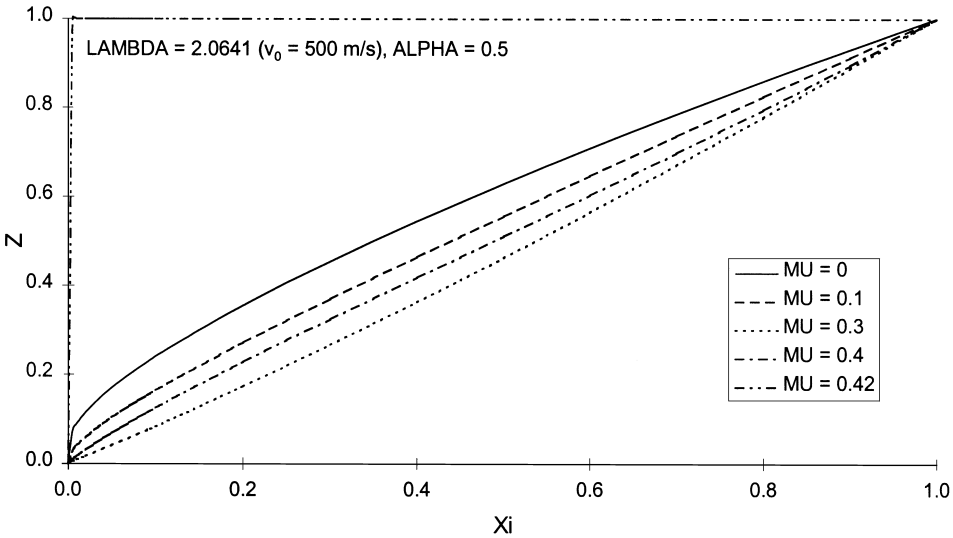

Fig. 4. Plots of optimal nose shape for $\alpha = 0.5$ and $\lambda = 2.0641$ ($v_0 = 500$ m/s) for various values of friction coefficient μ.

targets. These tests involved projectiles of mass 65 g and diameter 12.9 mm. The grout target force response coefficients were $A = 2.32\text{E}3$ kg/m^3 (target density) and $B = 281$ MPa (corresponding to $f_c' = 13.4$ MPa and a dynamic strength multiplier of 21). The numerical results involved selecting reasonable values of the system parameters α, λ, and μ for parametric studies.

Initially, a test case was conducted to determine if the formulation described in this paper indeed produced optimal penetration results. One means of accomplishing this is to compare the

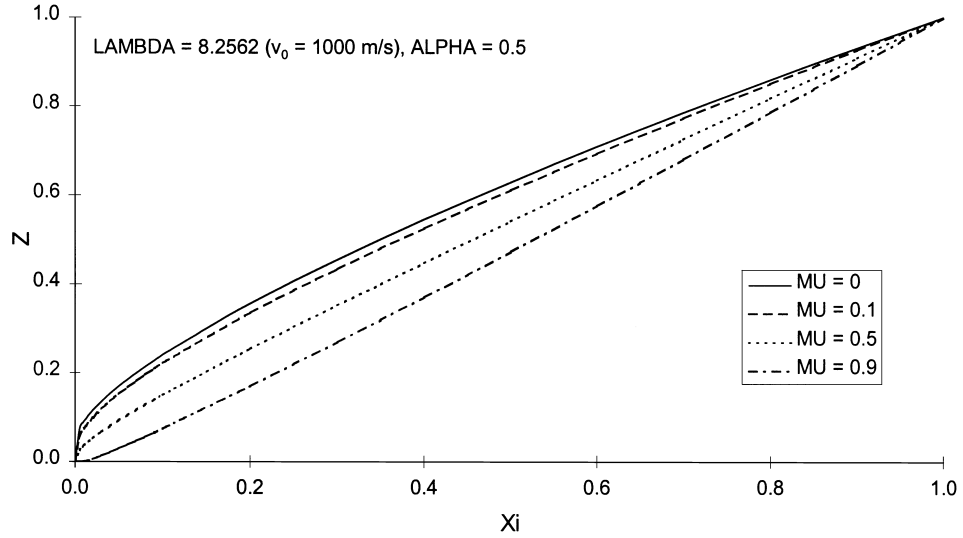

Fig. 5. Plots of optimal nose shape for $\alpha = 0.5$ and $\lambda = 8.2562$ ($v_0 = 1000$ m/s) for various values of friction coefficient μ.

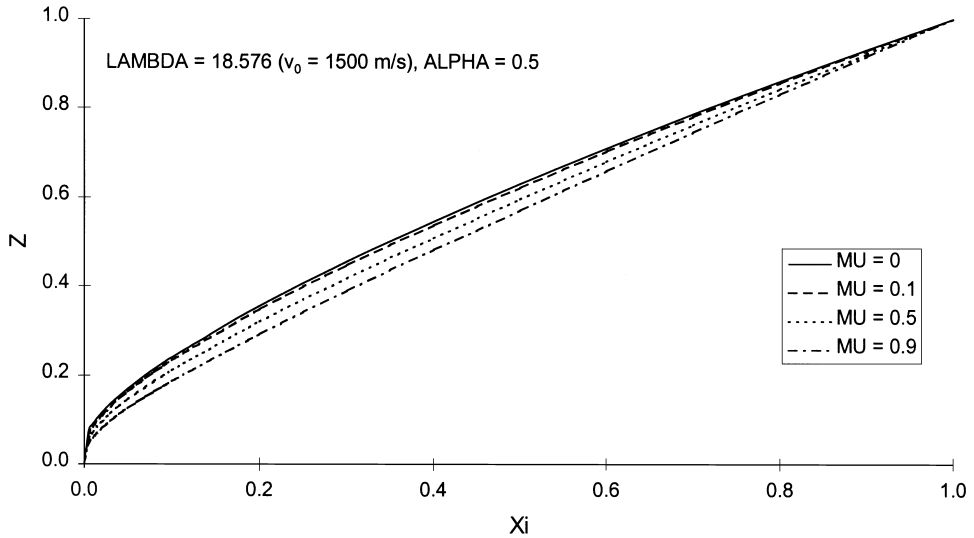

Fig. 6. Plots of optimal nose shape for $\alpha = 0.5$ and $\lambda = 18.576$ ($v_0 = 1500$ m/s) for various values of friction coefficient μ.

penetration depths of the optimal nose shape with a well-known effective nose shape — the ogive. Fig. 2 shows a plot of nondimensional penetration depth ($\bar{P} = 2\pi a^2 AN/m$) of optimal and ogival penetrators versus λ for $\alpha = 0.5$ and $\mu = 0.2$. As can be seen from this figure, the optimal penetrator is clearly more effective for the larger λ values. However, for λ values less than approximately 1.39 (lower-velocity impacts) the nature of the optimal solution changes completely. Instead of maximizing penetration depth minimization occurs and the optimizer drives the penetrator to a blunt-ended shape with penetration performance inferior to that of the ogive.

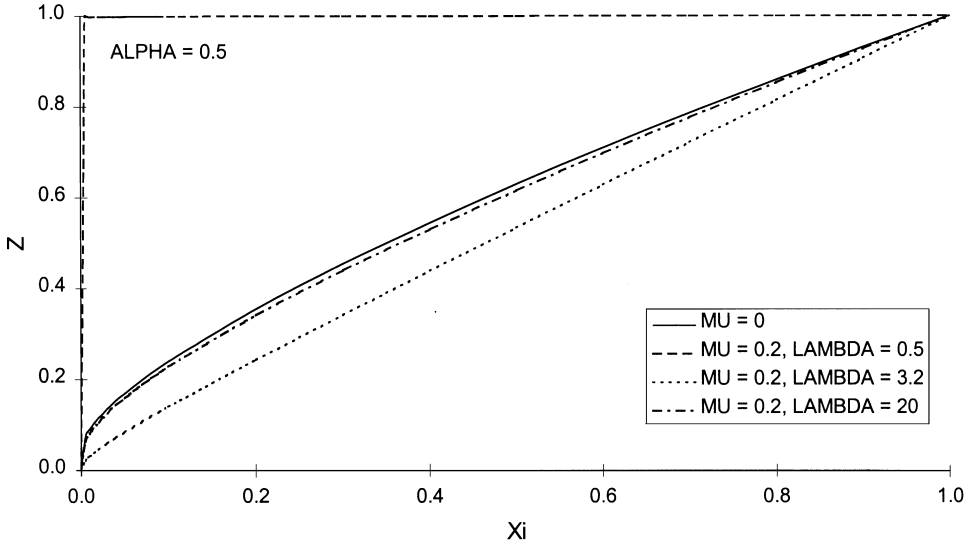

Fig. 7. Plots of optimal nose shape for $\alpha = 0.5$ and $\mu = 0.2$ for various values of λ. The frictionless case ($\mu = 0$) is shown for comparison.

Optimized nose shapes are compared with that of the frictionless case in Fig. 3. Further optimized nose shapes are shown in Fig. 4 [$\alpha = 0.5, \lambda = 2.0641$ ($v_0 = 500$ m/s)], Fig. 5 [$\alpha = 0.5, \lambda = 8.2562$ ($v_0 = 1000$ m/s)], and Fig. 6 [$\alpha = 0.5, \lambda = 18.576$ ($v_0 = 1500$ m/s)] for various friction coefficient μ levels. Note that at the higher impact velocities (Figs. 5 and 6) blunting did not occur even at very high friction levels.

Fig. 7 shows plots of optimal nose shape ($\alpha = 0.5, \mu = 0.2$) for various values of λ. The frictionless case ($\mu = 0$) is shown in this figure for comparison. Note that at low impact velocities (small λ) blunting occurs (penetration depth minimized) and that at high impact velocities the optimal shape closely resembles that of the frictionless case.

Critical levels of μ at which blunting occurs are plotted as a function of λ for various values of α in Fig. 8. This figure clearly shows that unrealistically large friction coefficients are necessary to cause a blunt penetrator solution at the higher impact velocities.

Finally, Fig. 9 compares optimal and ogival nose penetration performance as a function of λ for various values of α. In this figure optimal nose results were not plotted for those values of λ where blunting occurred.

7. Conclusions

In this paper, we have presented a variational analysis of normal penetration into semi-infinite targets including the effects of sliding friction on the tip of the penetrator. The choice of friction law for this paper was one of the simplest. However, the choice of friction may be simple, but its effect on the optimization problem is far from simple. Eq. (25) is a nonlinear differential–integral equation of staggering proportions and any form of analytical solution is practically impossible. The most

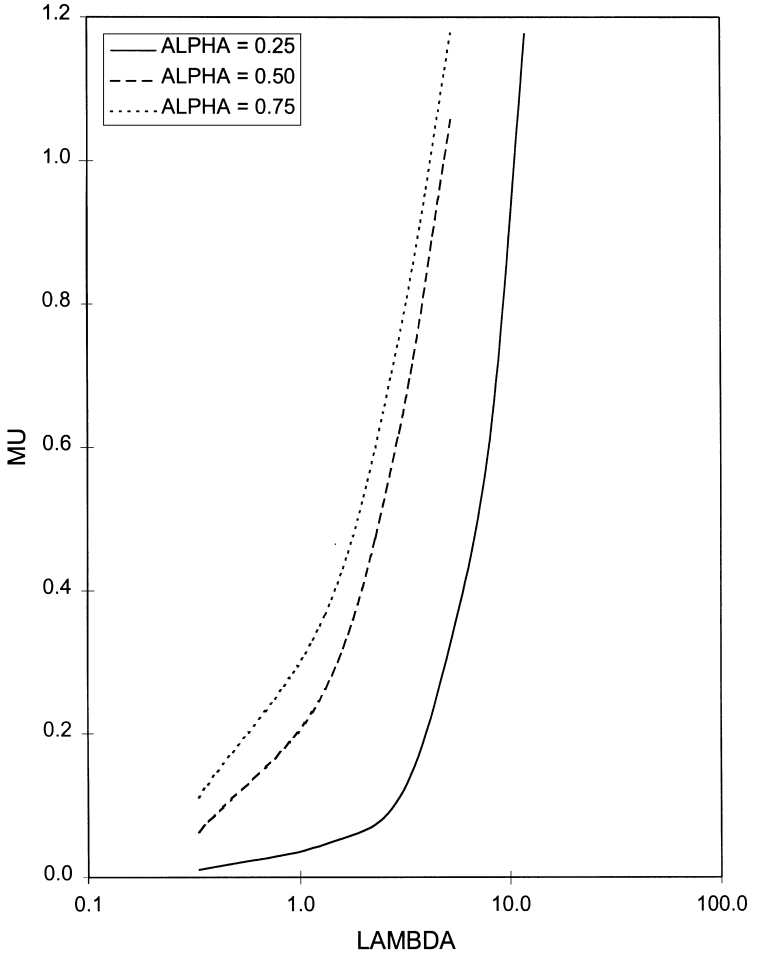

Fig. 8. Plots of the critical μ for blunting versus λ for various values of α.

expedient approach to solving the problem was to employ a weighted residual technique involving a trial solution that contained powers of the independent variable and four free constants chosen by an optimizer to minimize the residual error. This technique produced very satisfactory results when the combination of physical constants α, λ, and μ dictated a maximum for the variational integral. Except in the neighborhood of the transition to a minimum (conjugate point), the solution was stable and converged rapidly. After the transition to a minimum, the geometry predicted for the penetrator tip was as close to blunt-ended as possible (see Fig. 3). This situation in the variational calculus is not uncommon and is usually detected by examining the sign of the second variation. However, in this instance, that approach is practically impossible due to the severe complexity of the second variation.

The presence of friction alters the geometry for optimal performance at lower impact velocities by sharpening the nose of the projectile. The more friction that is present, the sharper the nose required to achieve maximum depth (of course, this assumes that no erosion is possible and the

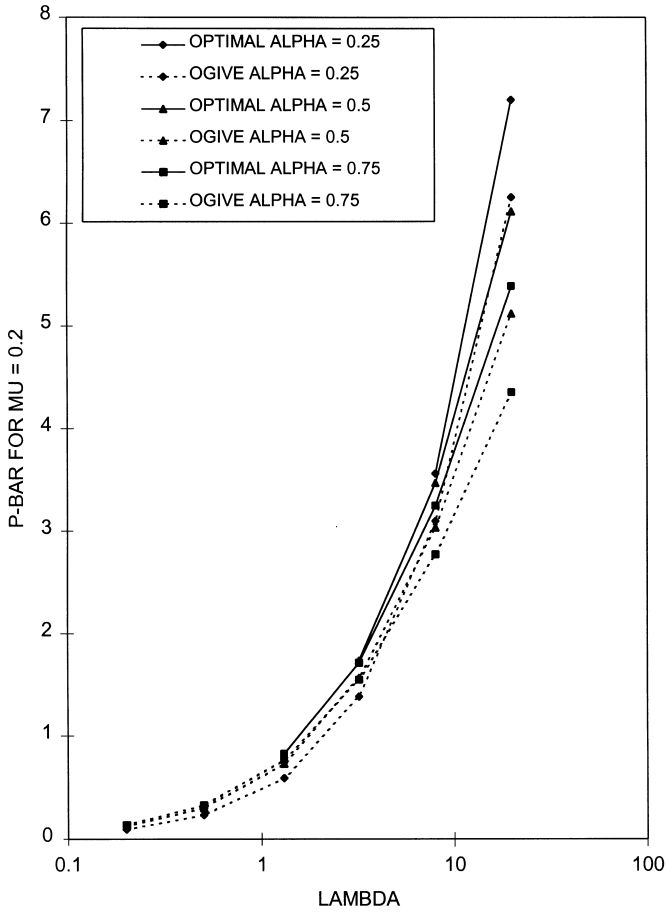

Fig. 9. Plots of $\bar{P}$ versus λ for optimal and ogival nose shapes for various values of α. Note that the optimal plots were stopped at the lower levels of λ where blunting occurred.

nose does not fail). However, for higher impact velocities, this sharpening of the nose only occurs for more friction than is reasonable to expect in these problems. For modest friction, the optimal nose geometry is very close to that predicted in the frictionless case. This is very good news indeed. Actual friction levels are extremely difficult to assess, making this analysis awkward to use in the design of a penetrator. This analysis does, however, provide us with qualitative insight into the penetration process and the role that friction plays for high- and low-velocity projectiles.

These conclusions should be verified by using an alternative friction law. This is the direction that future efforts in this area will take.

References

[1] Jones SE, Rule WK, Jerome DM, Klug RT. On the optimal nose geometry for a rigid penetrator. Proceedings of the International Symposium on Impact and Penetration Problems in Atlanta, GA, October, 1998, Comput Mech 1998;22:413.

[2] Poncelet JV. Cours de Mécanique Industrielle. Paris, 1829.
[3] Luk K, Forrestal MJ. Penetration into semi-infinite reinforced-concrete targets with spherical and ogival nose projectiles. Int J Impact Engng 1987;6(4):291.
[4] Backman ME, Goldsmith W. The mechanics of penetration of projectiles into targets. Int J Engng Sci 1978;16:1.
[5] Rinehart J, Pearson J. Behavior of materials under impulsive loads. New York: Dover, 1965.
[6] Bowden FP, Tabor D. The friction and lubrication of solids, Part II. London: Oxford University Press, 1964.
[7] Kragelskii IV. Friction and wear. Washington: Butterworths, 1965.
[8] Montgomery RS. Friction and wear at high sliding speeds. Wear 1976;36:275.
[9] Gaffney ES. Measurements of dynamic friction between rock and steel. DNA Report No. 4161F, 1976.
[10] Forrestal MJ, Grady DE. Penetration experiments for normal impact into geological targets. Int J Solids Struct 1982;18:229–34.
[11] Forrestal MJ, Frew DJ, Hanchak SJ, Brar NS. Penetration of grout and concrete targets with ogive–nose steel projectiles. Int J Impact Engng 1996;18(5):465.